Journal of
Micromechanics and
Microengineering

PAPER

An ultra-thin plate-level micropump with hydraulic-electromagnetic co-design methodology

To cite this article: Tianfeng Liu *et al* 2026 *J. Micromech. Microeng.* **36** 045016

IOP Publishing J. Micromech. Microeng. 36 (2026) 045016 https://doi.org/10.1088/1361-6439/ae5c13

Journal of Micromechanics and Microengineering

RECEIVED
24 March 2026

ACCEPTED FOR PUBLICATION
7 April 2026

PUBLISHED
28 April 2026

PAPER

An ultra-thin plate-level micropump with hydraulic-electromagnetic co-design methodology

Tianfeng Liu[1], **Song Xue**[1], **Weiwei Liao**[1], **Qi Chen**[2,*] **and Xiaobing Luo**[1,*]

[1] School of Energy and Power Engineering, Huazhong University of Science and Technology, Wuhan 430074, People's Republic of China

[2] Huake CoolCore (Shanghai) PowerTech Co., Ltd, Shanghai 200120, People's Republic of China

[*] Authors to whom any correspondence should be addressed.

E-mail: chenqi@hkcoolcore.com and luoxb@hust.edu.cn

Keywords: plate-level micropump, co-design methodology, microfluidic cooling, compact integration

Abstract

The advancement of high-power-density electronic devices imposes increasing demands on liquid cooling technology, in which the performance and size of the micropump are of paramount importance. For plate-level integrated applications, micropumps are required to possess both high performance and ultra-thin characteristics, a requirement that exceeds the capabilities of traditional decoupled hydraulic-electromagnetic designs. However, the transition to a co-design paradigm introduces new challenges. To address this, this paper proposes hydraulic-electromagnetic co-design methodology. The core of this method involves managing the dual bidirectional constraints—pertaining to both performance and geometric dimensions—between the hydraulic and electromagnetic components. The design process commences with the determination of preliminary hydraulic parameters based on the empirical coefficient method, followed by systematic characteristic matching and multi-round iterative optimization. Through this process, a high-performance, feasible design that balances hydraulic efficiency, electromagnetic performance, mechanical constraints, and manufacturability is efficiently identified, rather than pursuing a computationally prohibitive global optimum. An ultra-thin plate-level micropump prototype ($34 \times 34 \times 4.9$ mm^{-3}) fabricated based on this approach demonstrates a stable output of 100 ml min^{-1} flow rate at 13.05 kPa with merely 1 W power consumption.

1. Introduction

The rapid advancement of technologies such as artificial intelligence, high-performance computing, and 5G/6G communication has led to an exponential increase in the power density of electronic devices [1–5]. Consequently, thermal management has become a critical bottleneck limiting system performance, reliability, and longevity. Among various cooling solutions [6–8], liquid cooling is widely regarded as the necessary path forward for next-generation high-heat-flux chips due to its superior heat removal capacity [9–11].

The effectiveness of a liquid cooling system hinges on its core driving component—the micropump [12, 13]. For plate-level integration scenarios, spatial constraints are extremely severe, demanding that micropumps deliver sufficient hydraulic performance while maintaining an ultra-thin form factor [14, 15]. For a 15 W thermal design power ultra-thin laptop as an example, its chassis thickness is typically less than 15 mm. Therefore, to maintain the CPU core temperature within the range of 75 °C–85 °C, the total thickness of the micropump must be controlled within 5 mm, and the planar dimensions should be less than 40×40 mm^{-2}. Additionally, to overcome the flow resistance of the microchannel cold plate and the ultra-thin heat exchanger, the micropump must provide pressure head above 10 kPa while sustaining a stable flow rate above 80 ml min^{-1}. Table 1 lists several micropumps with thickness on the order of 10 mm, which can be broadly categorized into non-mechanical and mechanical pumps. Non-mechanical pumps are primarily used in microfluidics for applications requiring precise fluid

Table 1. Several micropumps with a thickness on the order of 10 mm.

Designer	Pump type	Size (mm^3)	Flow rate (ml min^{-1})	Pressure head (kPa)
Zhou and Amirouche [18]	Electromagnetic	20 × 12 × 3.5	0.3196	0.931
Chia *et al* [19]	Thermo-pneumatic peristaltic	16 × 18 × 5	0.0201	0.49
Mousoulis *et al* [20]	Phase-change	14 × 14 × 8	0.0288	28.9
Nguyun *et al* [21]	Electroactive polymer	20 × 20 × 5	0.76	1.5
Ma *et al* [22]	Piezoelectric	50 × 50 × 12	250	10
Feng and Kim [23]	Piezoelectric	13 × 13 × 1.2	0.7	4
Munas *et al* [24]	Piezoelectric	100 × 60 × 5.5	30.72	0.245

control and therefore cannot meet the driving requirements of micro-liquid cooling systems. Mechanical pumps are mainly divided into two types: reciprocating and rotary. Reciprocating mechanical pumps, represented by piezoelectric pumps, can drive micro-liquid cooling systems with minimal thickness. However, their long-term operational reliability needs improvement due to fatigue issues. Conventional design of motor-driven rotary mechanical pumps [16, 17] typically follows a sequential paradigm: the hydraulic components (e.g. impeller and volute) are first designed and optimized based on target performance, after which a motor is selected or sized to meet the torque-speed requirements of this predefined hydraulic load. This decoupled approach, while straightforward, inherently limits system-level optimization. When pushing for extreme form factors—such as sub-10 mm thickness—this paradigm reaches a bottleneck: the fixed hydraulic geometry severely constrains the electromagnetic design space, often forcing the motor to operate inefficiently and leading to significant performance compromise.

To break this fundamental limitation, we propose and implement a hydraulic-electromagnetic co-design paradigm. The core of this approach is to treat the hydraulic and electromagnetic subsystems as a deeply coupled system from the outset. Their key design parameters are optimized simultaneously, with the bidirectional constraints—where hydraulic geometry dictates electromagnetic space, and electromagnetic performance governs hydraulic loading—being explicitly managed as integral parts of the problem. This allows for the discovery of unconventional design solutions that balance overall performance within stringent spatial constraints, a task that is intractable under the traditional sequential design framework. The primary challenge, and the focus of this work, is to systematically model and navigate this complex, coupled design space.

This paper proposes a hydraulic-electromagnetic co-design methodology for an ultra-thin plate micropump to address the above challenges. The core of our work lies in systematically handling and optimizing these dual bidirectional constraints. The design process begins with determining preliminary hydraulic parameters based on an empirical coefficient method. Subsequently, a parametric matching and iterative optimization workflow is established to screen a wide range of feasible hydraulic and electromagnetic parameter combinations. Based on this optimized design, we fabricated a prototype of the ultra-thin plate micropump. Experimental results demonstrate that the prototype achieves expected hydraulic performance while possessing a minimal thickness, thereby validating the effectiveness and superiority of the proposed co-design approach.

2. Structure and working principle

Figure 1(a) shows the cross-sectional structure of our ultra-thin plate micropump [20–25]. The pump cover and pump base together form the pump housing, with their internal cavities constituting the pump chamber. The stator is located on the external side of the pump housing and connected to the driver board, while the rotor, combined with the bearing and the impeller blades, forms the impeller. Differing from conventional designs where power is transmitted via a motor shaft with dynamic seals, our design features a central shaft fixed to the base. This fixed shaft, along with the bearing mounted on the rotor, provides radial and axial constraint to the impeller. Static sealing is achieved using sealing rings placed in capillary groove. Since the pressure inside the pump chamber is only on the order of tens of kPa, static sealing is sufficient to ensure reliable sealing. To further minimize the overall pump thickness, the inlet and outlet ports are located on the side of the base. From the initial design stage, practical machining and assembly considerations must be taken into account.

Figures 1(b) and (c) detail the radial and axial constraints of the impeller. The center O_1 of the central shaft is fixed relative to the pump chamber. When the center O_2 of the bearing is offset from O_1 by a distance e, the minimum clearance $h_{\min}$ between the bearing and the shaft occurs along line O_1O_2. At this position, the bearing experiences a surface contact pressure P_s from the shaft, which

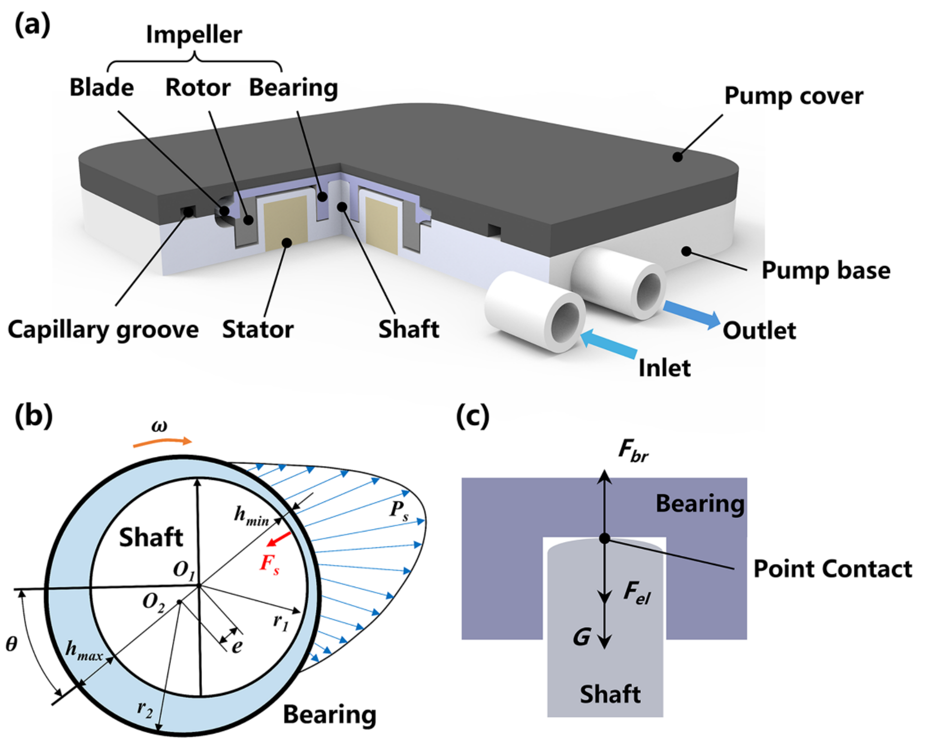

Figure 1. Structure of the ultra-thin plate micropump. (a) The cross-sectional structure of the micropump. (b) Radial constraint diagram of the impeller. (c) Axial constraint diagram of the impeller.

influences its direction of movement. This interaction repeats, forming the radial constraint on the impeller. The end face of the shaft is designed as a spherical surface to create point contact with the bearing end face, thereby minimizing the contact area and reducing the rotational resistance imposed by the shaft on the impeller. For axial constraint, since the motor stator and rotor are placed on opposite sides of the base, their magnetic centers are not coaxial. This results in a downward magnetic force F_{el} on the impeller, as shown in figure 1(c). This force, together with the impeller's weight G and the supporting force F_{br} from the shaft, constitutes the axial constraint on the impeller. In conventional designs, the motor and hydraulic components are separated, and shaft support issues are transferred to the interior of the motor. Axial constraints do not rely on magnetic pull, which substantially differs from our designed micropump. In practical manufacturing, the magnitude of axial and radial clearance depends on machining processes and assembly accuracy. Based on the axial and radial constraint structure we proposed, we employ wear-resistant and corrosion-resistant ceramic shafting to ensure system reliability after prolonged rotor operation.

Upon energization, the stator generates an alternating magnetic field driven by electrical signals. The rotor, induced by this field, drives the impeller to rotate, which does work on the fluid entering the pump chamber, ultimately discharging pressurized fluid from the outlet. To prevent any changes in pump chamber components due to corrosion, all non-electromagnetic parts are fabricated from plastic, while all electromagnetic-related components undergo surface treatment. This approach ensures both precision and corrosion resistance requirements are met.

3. Methods

3.1. Hydraulic design

Due to the distinctive working principle of the vortex pump and the intricate internal flow process, it is not feasible to achieve both precise and efficient design through a single approach. Hence, we adopted a combination of the empirical coefficient method [26] and CFD simulation to carry out the hydraulic design of the vortex pump.

Figure 2(a) shows the specific hydraulic process. First, we need to deduce the performance requirements of the micropump based on the needs of liquid cooling system. Subsequently, an initial rotational

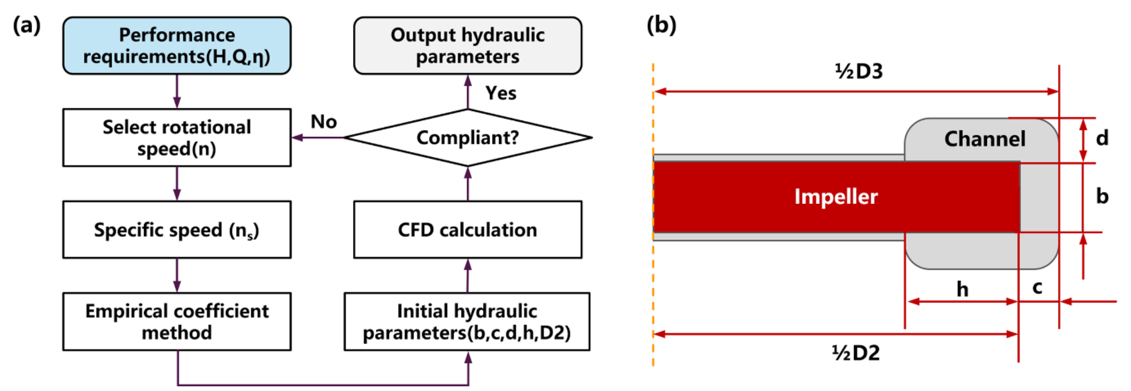

Figure 2. Hydraulic design method. (a) Hydraulic design process. (b) Main parameters of hydraulic model.

speed should be selected, and the specific speed is calculated using the formula provided below:

$$n_s = \frac{3.65 \times n \times \sqrt{Q}}{H^{3/4}} \tag{1}$$

where n represents the actual rotational speed of the pump impeller, Q stands for the output flow rate of the pump, H indicates the output head. Specific speed is a critical dimensionless parameter in fluid machinery, used to compare geometrically similar pumps and fans with different operating parameters. Following this, the empirical coefficient method is employed to calculate the initial hydraulic parameters, with the key parameters—including the geometric dimensions of the impeller and flow channel—presented in figure 2(b). The empirical coefficient method is based on a series of pumps with excellent performance, summarizing empirical formulas that describe the relationship between various coefficients, whose specific expressions are provided as follows:

$$D = \frac{84.6}{n}\sqrt{\frac{H}{\psi}} \tag{2}$$

$$v = K_v u \tag{3}$$

$$A = \frac{Q}{\eta_v v} \tag{4}$$

$$b = k\left(\frac{Q}{\eta_v K_v}\right)^{1/2}\left(\frac{\psi}{H}\right)^{1/4} \tag{5}$$

where D is impeller outer diameter, v is average liquid velocity, A is flow channel area, b is impeller width, n represents the actual rotational speed of the pump impeller, Q stands for the output flow rate of the pump, H indicates the output head, ψ is the head coefficient, K_v is the flow channel velocity coefficient, and k is the impeller width coefficient. The value of ψ typically falls within the range of 0.6–1.4, where lower values correspond to higher specific speed and higher rotational speed. For the rectangular flow channel shown in figure 2(b), empirical formulas are as follows:

$$c = (0.25 - 0.5)\,b \tag{6}$$

$$d = (0.4 - 0.6)\,b \tag{7}$$

$$h = (0.9 - 1.2)\,b. \tag{8}$$

Preliminary parameter selection can be based on taking intermediate values within their respective ranges. The number of blades has a significant impact on pump performance. As the number of blades increases, the pressure head rises notably, and power consumption also increases slightly. When the number reaches a certain threshold, pressure head, efficiency and power consumption remain largely

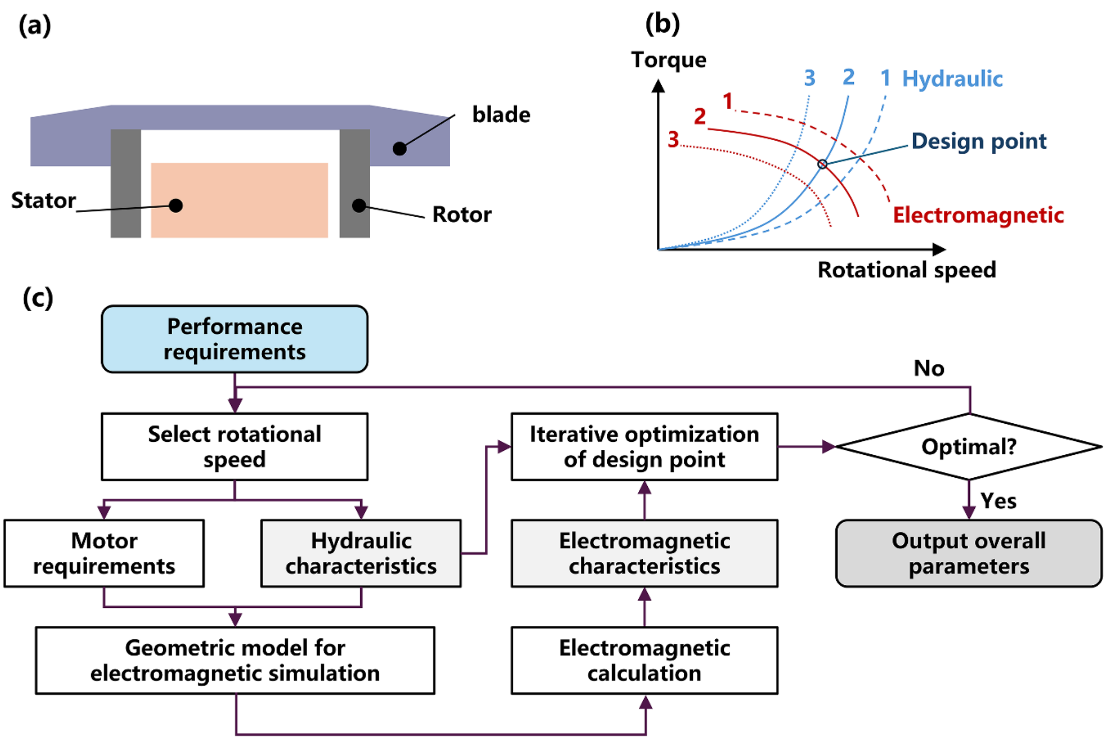

Figure 3. Hydraulic-electromagnetic co-design content and process. (a) Synergistic relationship between hydraulic and motor components. (b) Hydraulic-electromagnetic performance matching diagram. (c) Collaborative design process.

unchanged. Further increasing the blade count will lead to higher torque and reduced efficiency. Typically, the number of blades ranges from 30 to 60. For preliminary selection, we have chosen a blade count of 41.

Next, we construct a geometric model for hydraulic simulation using the initial hydraulic parameters and perform CFD calculations. The influence of the shaft on the performance of rotating machinery is generally minor. Therefore, simulations typically simplify the shaft. If the performance meets the requirements, the hydraulic parameters are output. Otherwise, the rotational speed is adjusted, and a new round of calculations is conducted until the performance meets the required specifications.

3.2. Hydraulic-electromagnetic co-design

Following the completion of the hydraulic design, a family of hydraulic parameters that meet the performance requirements can be obtained. Subsequently, the selection of optimal parameters from this family necessitates a synergistic design approach integrating hydraulic and motor components. Figure 3(a) shows a schematic diagram of the co-operative relationship between the hydraulic and motor components. The stator, rotor and impeller blades must be concentric and rotate together about the shaft. The rotor is shaped as a hollow cylinder, which can be formed either as an assembly of magnet segments mounted on a magnetic steel back-iron or as a single-piece bonded magnet ring. The one-sided clearance between the stator and rotor is called the air gap. The air gap is determined by the wall thickness and the safety margin reserved for rotor eccentricity. We can tell from figure 3(a) that two critical dimensions of coupling are identified: performance coupling and geometric coupling. In terms of performance coupling, the hydraulic and motor components share identical rotational speed and torque during operation. Regarding geometric coupling, owing to the adoption of a co-planar design combined with an outer-rotor brushless motor topology, the inner diameter of the impeller is equivalent to the outer diameter of the motor rotor.

Via CFD simulations and electromagnetic simulations, the torque-rotational speed characteristics of the hydraulic and motor components are obtained, as presented in figure 3(b). The intersection of these two characteristic curves corresponds to the design point of the integrated system. If the actual operating point exceeds this design point, the system will exhibit an increased physical footprint, elevated power consumption, and reduced operational efficiency. Conversely, should the operating point fall below the design point, performance requirements will not be met, accompanied by diminished efficiency. Strong interactions between parameters are indeed central to the design challenge. For instance, a configuration with a smaller impeller diameter and larger blade height may enhance hydraulic efficiency but concurrently reduces the electromagnetic force coupling between the rotor and stator, potentially degrading motor performance. It is precisely due to these complex, competing trade-offs that a hydraulic-electromagnetic co-design approach is essential to systematically navigate the design space and prevent sub-optimization in any single domain.

Figure 3(c) illustrates the co-design process. First, the rotational speed is selected based on the performance requirements. Subsequently, the hydraulic design method is employed to derive the motor specifications and the corresponding hydraulic characteristic parameters. Next, a geometric model for electromagnetic simulation is established, and electromagnetic simulations are performed to obtain the electromagnetic characteristic parameters. These hydraulic and electromagnetic parameters undergo multiple rounds of iterative optimization before it offers a balanced, high-performance outcome that meets our target specifications. Otherwise, the rotational speed is reselected to ensure the attainment of optimal parameters. The proposed method fundamentally redefines impeller diameter and magnet ring diameter. The fundamental constraint of the traditional decoupled design approach lies in conducting hydraulic and electromagnetic designs within two independent constraint spaces, and each of them aims for optimal performance within its own domain. For instance, hydraulic design seeks to minimize the impeller diameter to enhance the pressure head. However, this unilaterally imposes a fixed boundary condition on the electromagnetic design, forcing the motor to operate in an inefficient region. The optimization process also took into account parameters affecting stator performance. For example, the thickness of the winding wire must balance the overall performance of the stator windings with the spatial compatibility between the wound stator's total volume and the stator slots. As this aspect pertains more to manufacturing processes, it will not be elaborated on further in this paper. Our co-design methodology transforms such fixed constraints into co-optimization variables.

4. Results and discussions

4.1. Modeling validation

To validate the accuracy of the empirical parameter method, geometric modeling of the micropump's fluid domain was conducted, as illustrated in figure 4(a). The model comprises the impeller, flow channel, inlet port, and outlet port. Due to the complex internal structure of the pump, structured grid generation is challenging; thus, tetrahedral unstructured grids with strong adaptability were employed. For hydraulic calculations, the sliding mesh technique was adopted, dividing the entire computational domain into dynamic and static regions. An interface-coupled wall was set between these two regions to enable numerical data transfer, ensuring computational accuracy. Results of grid generation and grid independence verification are presented in figure 4(b). The generated grids were imported into Ansys Fluent for calculations, with the specific numerical solution scheme as follows: The Reynolds-averaged Navier–Stokes equations were solved, employing the k–ε turbulence model and no-slip wall conditions. Second-order upwind schemes were used for discretization to ensure calculation accuracy of dynamic and turbulent terms. The SIMPLE solver was adopted, with the convergence criterion for algorithm residuals set to 0.001%. At the inlet, a velocity boundary condition is applied according to the specified flow rate. The outlet is modeled as an outflow boundary. The pressure head generated by the pump is calculated as the difference between the area-averaged total pressure at the outlet and that at the inlet. Under a rotational speed of 6000 rpm, grid counts of 3.69 million, 4.15 million, 5.46 million, 6.16 million, 7.60 million, and 8.61 million were tested. It was observed that when the grid count reached 6.16 million, the calculated head error did not exceed 1%. Consequently, this grid configuration was selected for all remaining CFD model calculations.

Similarly, figures 4(c) and (d) presents the geometric model and grid independence verification of electromagnetic simulation, respectively. Electromagnetic simulation model consists of stator core, coil, impeller, steel magnet and motor housing. The torque-time variation curves in figure 4(d) are compared for grid numbers of 90 482, 169 861 and 258 204, respectively. It can be seen that the grid number of 90 482 is already relatively accurate, so this grid division method is adopted for subsequent electromagnetic simulation calculations.

4.2. Simulation results

Following the procedure and methods outlined in sections 3.1 and 3.2, a preliminary hydraulic model was obtained. The hydraulic-electromagnetic co-design methodology was then applied to perform multiple iterative matching cycles between the hydraulic and electromagnetic components. In our computational case study, we performed 20–30 iterations to reach the optimal solution. The actual iteration

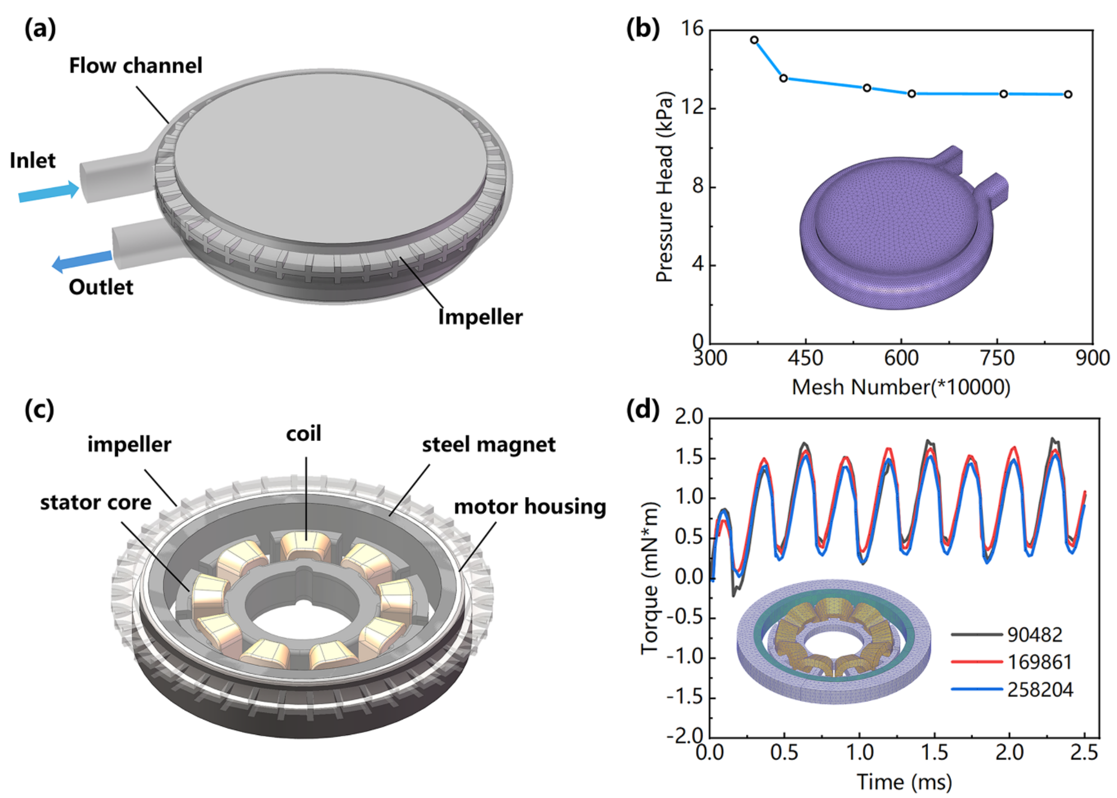

Figure 4. Simulation model and verification of grid independence. (a) Hydraulic geometric model. (b) Validation of CFD grid independence. (c) Electromagnetic simulation geometric model. (d) Validation of electromagnetic simulation grid independence.

Table 2. Design parameters and results of the original model, optimized range and optimized model.

Model	Original	Optimized range	Optimized
Diameter $D2$ (mm)	17.66	18	18
Blade width b (mm)	1.1	0.8–1.2	1
Flow channel c (mm)	0.36	0.25–0.6	0.4
Flow channel d (mm)	0.66	0.35–0.7	0.5
Blade height h (mm)	0.65	0.8–1.2	1
Number of blades z	41	30–60	41
Axial clearance δ_1 (mm)	0.1	0.1–0.2	0.1
Radial clearance δ_2 (mm)	0.1	0.1–0.2	0.1
Baffle tongue angle θ (°)	80	80	80
Rotor outer diameter r_o (mm)	15.76	D2-2h-0.6	15.4
Rotor inner diameter r_i (mm)	13.4	—	13.2
Stator outer diameter s_o (mm)	12.6	rr-2δ_2 -0.6	12.4
Stator inner diameter s_i (mm)	5.4	5.4	5.4
Bearing outer diameter (mm)	4	4	4
Rotational speed (rpm)	6000	4000–7000	6000
Torque (mN * m)	0.84	—	0.77
Flow rate (ml min^{-1})	100	—	100
Pressure head (kPa)	11.5	—	15.01
Hydraulic efficiency (%)	3.63	—	5.17
Motor efficiency (%)	0.38	—	0.45
Pump efficiency (%)	1.38	—	2.33

count depends on the selected empirical coefficients. These coefficients need fine-tuning for different operating conditions. Therefore, when the performance requirements for the micropump change, the number of iterations will also vary. The design parameters and simulation results of the original model, optimized range and optimized model are listed in table 2. In common engineering design, parameters are typically rounded to integers for manufacturing considerations. Therefore, during the optimization process, we manually rounded each parameter to its nearest integer.

The original design parameters had yielded relatively excellent performance, with operating characteristics already quite close to the target. Further optimization only requires fine-tuning of parameters within a small range. The number of blades z ranges from 30 to 60. Results show that as the blade count increases, the pressure head and efficiency improve slightly, while torque increases accordingly. The efficiency gain is more significant between 30 and 40 blades, becoming gradual from 40 to 60. Given that a higher blade count increases manufacturing difficulty and to avoid resonance with the blade pass frequency and its harmonics, 41 blades were selected as the optimal number. Keeping other parameters constant, the axial clearance δ_1 and radial clearance δ_2 were varied independently within 0.1–0.2 mm range. The simulations revealed the increasing clearance leads to a sharp decline in both pressure head and hydraulic efficiency. Therefore, the clearance should be minimized to the lowest value permissible by manufacturing and assembly tolerances, and this leads to selection of 0.1 mm as the optimal clearance. Blade width b, Blade height h, Flow channel c and Flow channel *d* are the key factors determining the performance. These four parameters exhibit a certain degree of coupling. Studying this complex interdependence through single-parameter analysis is challenging, because it requires iterative optimization based on the influence relationships of individual parameters. Since blade parameters have greater impact on performance, the iteration should prioritize blade parameters. The other parameters can be studied by establishing proportional relationships with blade parameters. To maintain the strength of structural components, the minimum wall thickness is set at 0.3 mm. Consequently, the following relationships are established: the rotor outer diameter ro and Diameter D2 are related by r_o = D2-2h-0.6. The stator outer diameter so and rotor inner diameter r_i are related by s_o = rr-2δ_2-0.6. The bearing outer diameter adopts 4 mm specification, which is common in ultra-thin fans.

The results show that the optimized model demonstrates superior performance along with improved efficiency. Although the optimized structure appears to differ only slightly from the pre-optimized version, it is worth noting that significant dimensional reduction is challenging to achieve when the structure is already very thin. The optimization results confirm that our method effectively achieves the goal of co-design. Moreover, our methodological framework is scalable to thicknesses of 5 mm and 3 mm based on the proposed method. For even smaller dimensions, limited by machining and assembly precision, we believe that the micropump structure we designed may not have a performance advantage over other types of pumps (such as piezoelectric pumps). However, the method itself still holds certain guiding significance.

Subsequently, an analysis of the pressure and velocity fields before and after optimization was conducted. Figure 5 presents the pressure and velocity fields on the cross-sectional plane of the impeller for both cases, with the impeller rotating clockwise as indicated. Specifically, figures 5(a) and (c) display the pressure and velocity fields of the initial design, while figures 5(b) and (d) correspond to the optimized design. The pressure field distribution shows that the fluid pressure gradually increases from the inlet to the outlet as work is imparted by the rotating blades. A rapid pressure drop is observed within the tongue region from the outlet back towards the inlet. A comparative analysis of figures 5(a) and (b) reveals that the pressure rise along the flow path is slower in the initial design compared to the optimized one, where the pressure increases more rapidly. Comparing figures 5(c) and (d), the average fluid velocity within the flow passages is significantly higher in the optimized structure. In the initial design, the slower velocity at the outlet results in less intense fluid-wall interaction after the fluid leaves the impeller, leading to relatively lower losses. However, the optimized structure imparts more energy to the fluid. The overall performance gain from this increased energy transfer outweighs the associated losses, resulting in enhanced performance and efficiency.

Figure 6 shows the matching curves between the electromagnetic driver and the hydraulic components. Figure 6(a) depicts the torque-speed matching curve. It can be observed that the torque required by the hydraulic components increases with rotational speed, while the torque provided by the electromagnetic driver gradually decreases. The two curves intersect at a speed slightly above 6000 rpm, a point designed with a 10% engineering margin to ensure that the driver's output torque adequately meets the hydraulic demand at the target operating speed of 6000 rpm. Figure 6(b) presents the efficiency-speed curves for both the hydraulic and electromagnetic components. The efficiency of both components initially increases and then decreases with rising speed. Through the adjustment method described in section 3.2, the peak efficiency points of both components were aligned at the target operating point (6000 rpm).

4.3. Experimental results

Figure 7(a) illustrates the schematic of the flow loop used to evaluate the hydraulic performance of the micropump. In this system, the pump draws fluid from a water tank, and the flow rate is measured by a flow meter. The fluid is then returned to the water tank, completing a closed cycle. Pipeline resistance

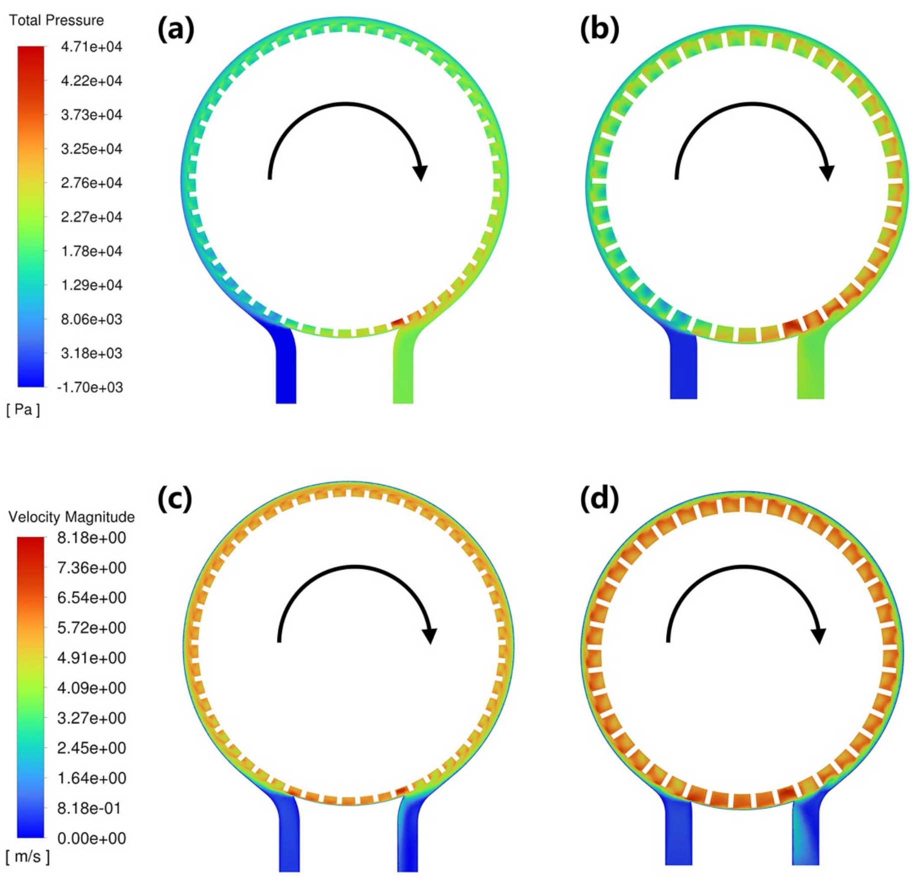

Figure 5. Comparison of the hydraulic model before and after optimization. (a) Original pressure distribution. (b) Optimized pressure distribution. (c) Original velocity distribution. (d) Optimized velocity distribution.

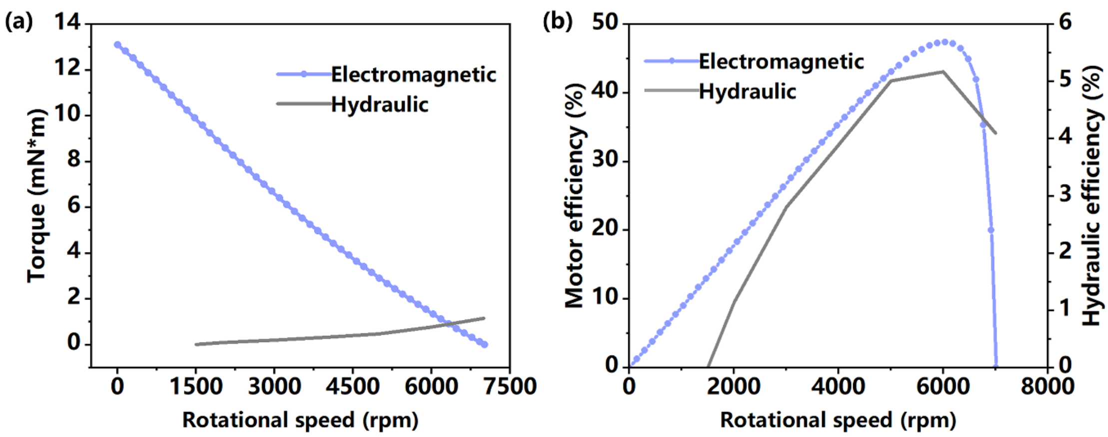

Figure 6. The matching curve of hydraulic and electromagnetic. (a) The matching curve of torque-rotational speed. (b) The matching curve of efficiency-rotational speed.

is adjusted by a valve, allowing the pump to be tested under various flow conditions. The pressure head generated by the pump is accurately measured by a differential pressure gauge connected to its inlet and outlet.

Figure 7(b) shows a photograph of the experimental setup, which includes two DC power supplies (one for driving micropump, the other for driving flowmeter), a micropump controller, and the flow metering system. The testing procedure was as follows: First, the micropump was installed in the test loop, ensuring the correct flow direction. After filling the water tank with purified water, the system was thoroughly purged of air to ensure complete priming—a crucial step as the vortex pump impeller

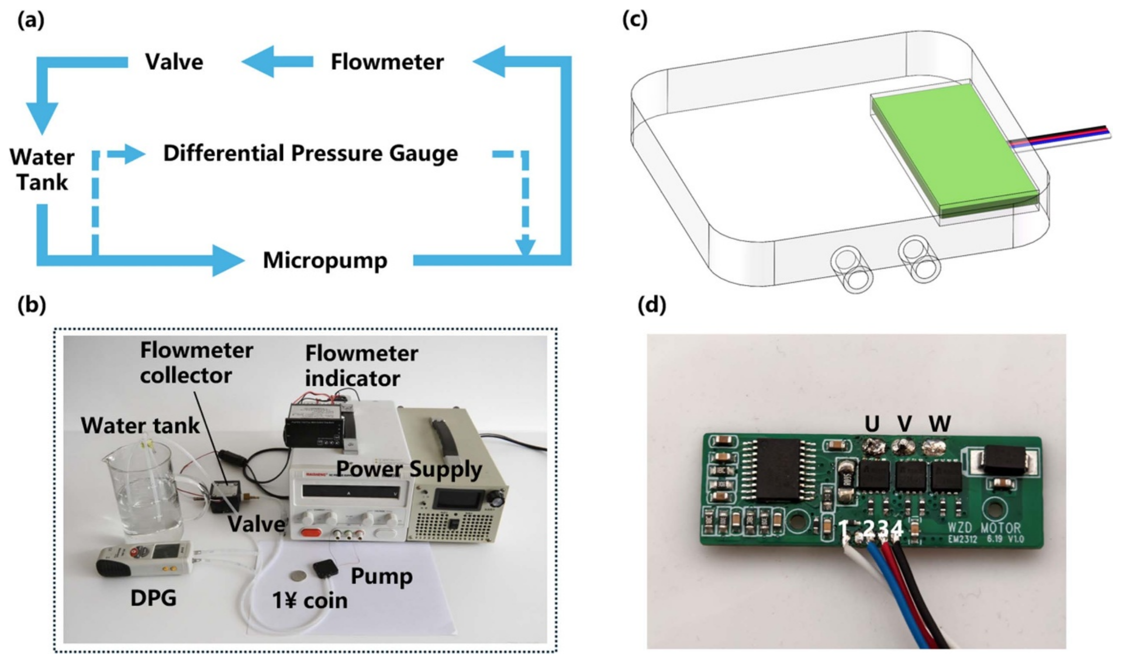

Figure 7. Experimental setup. (a) Flow loop schematic of experimental system. (b) Physical diagram of the hydraulic performance test. (c) The relative position of the driver board in the micropump. (d) The physical diagram of the driver board.

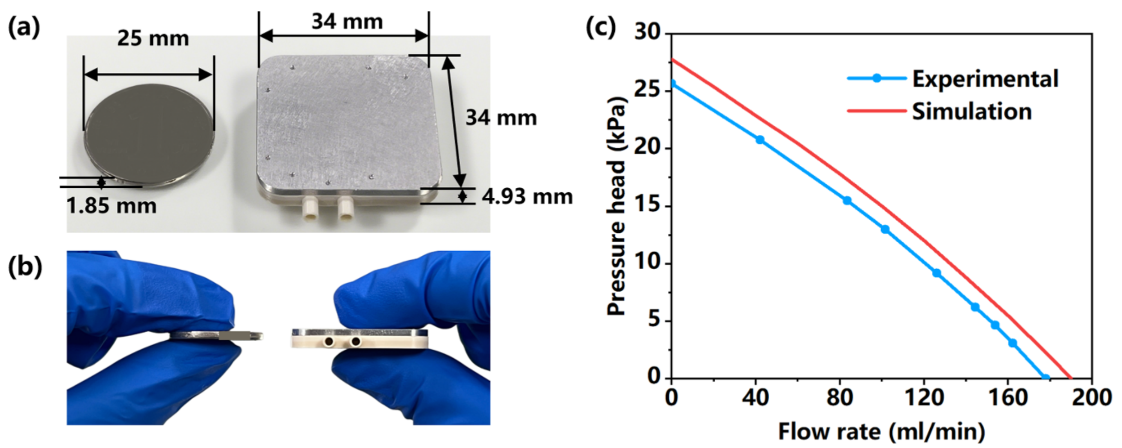

Figure 8. Experimental results. A comparison of the prototype and 1-yuan coin-shape object in the (a) horizontal direction and (b) thickness direction. (c) P–Q results comparison between simulation and experiment.

lacks self-priming capability. The non-self-priming characteristic of the micropump may lead to various reliability issues. For example, excessive pre-fill loss could cause the rotor to idle, subsequently paralyzing the entire liquid cooling loop. Therefore, to prevent such occurrences, corresponding measures must be taken to eliminate pre-fill loss. For system-integrated applications, priming failure is mitigated through system-level design measures. The fluid loop is vacuum filled during manufacturing, the pump is placed at the lowest point of the loop, and a venting mechanism is incorporated at the high point to exhaust any trapped gas. In experimental setups, prior to operation, the inlet tube is immersed in the water tank, and a syringe is used to draw water repeatedly from the outlet until the entire fluid circuit is fully liquid-filled. The driver board is integrated in the area shown in figure 7(c). Apart from the leads, the rest of the PCB does not extend beyond the micropump's volume. Figure 7(d) is a photograph of the driver board, where *U*, *V*, and *W* are soldered to the three leads of the stator winding. Contacts 1, 2, 3, and 4 correspond to the FG signal output line, PWM speed-control line, positive terminal, and negative terminal, respectively. With the power supply set to 6 V, the system was activated. The valve was then adjusted to vary the flow rate, and the corresponding head and flow rate data at each operating point were recorded.

Table 3. Hydraulic performance test of the micropump.

Flow rate	Pressure head	Voltage	Current	Power consumption
ml min^{-1}	kPa	V	A	W
178	0	6.01	0.155	0.931 55
162.2	3.15	6.01	0.156	0.937 56
153.9	4.63	6.01	0.156	0.937 56
144.5	6.23	6.01	0.158	0.949 58
126	9.18	6.01	0.159	0.955 59
101.6	13.05	6.01	0.161	0.967 61
83.5	15.50	6.01	0.163	0.979 63
42.1	20.85	6.01	0.166	0.997 66
0	25.70	6.01	0.17	1.0217

Figure 8 presents the fabricated prototype of our micropump and a comparison of its performance with simulation results. Figures 8(a) and (b) provide top and side views, respectively, of the prototype alongside a Chinese 1-yuan coin-shape object (25 mm diameter, 1.85 mm thickness) for size reference. The overall dimensions of the prototype are 34 mm × 34 mm × 4.9 mm (excluding the protruding tube length). Table 3 shows the hydraulic performance test results of our micropump. Figure 8(c) shows simulation and experiment results at a rotational speed of 6000 rpm. The simulation predicts a maximum flow rate of 190 ml min^{-1} and a maximum head (at shut-off) of 27.8 kPa. The experimentally measured values are 178 ml min^{-1} and 25.7 kPa, respectively. At a flow rate of 100 ml min^{-1}, the simulated and measured heads are 15.01 kPa and 13.05 kPa and indicative power consumption is 0.97 W. Meanwhile, the noise level at 0.3 m from the micropump is 24.8 dBA, which is significantly lower than the fan noise of traditional ultra-thin laptops operating under full load (>30 dBA). Although the experimental values are slightly lower than the simulations across all operating points, the close parallelism of the two curves indicates that the simulation model accurately captures the performance trends of the micropump.

5. Conclusions

This study successfully developed an ultra-thin plate micropump for plate-level liquid cooling of high-power-density electronic devices. By introducing a novel hydraulic-electromagnetic co-design paradigm, the core challenge of dual bidirectional constraints between the hydraulic and electromagnetic components in both performance and geometric dimensions was overcome. The fabricated prototype, with a compact form factor of 34 mm × 34 mm × 4.9 mm, demonstrates superior hydraulic performance while maintaining an ultra-thin profile. The close agreement between experimental and simulation results validates the effectiveness and superiority of the co-design approach in achieving the synergistic optimization of high performance and miniaturization in micropumps, offering a new direction for next-generation micropump development.

Acknowledgments

This work is supported by Science Challenge Project (No. TZ2025004).

Data availability statement

The data cannot be made publicly available upon publication because no suitable repository exists for hosting data in this field of study. The data that support the findings of this study are available upon reasonable request from the authors.

Conflict of interest

The authors declare that they have no known competing financial interests or personal relationships that could have appeared to influence the work reported in this paper.

Author contributions

Tianfeng Liu
Conceptualization (equal), Formal analysis (equal), Methodology (equal), Writing – original draft (equal)

Song Xue
Formal analysis (equal), Validation (equal)

Qi Chen
Funding acquisition (equal), Project administration (equal), Supervision (equal), Writing – review & editing (equal)

Xiaobing Luo 0000-0002-6423-9868
Funding acquisition (equal), Project administration (equal), Supervision (equal), Writing – review & editing (equal)

References

[1] Zhang Z, Wang X and Yan Y 2021 A review of the state-of-the-art in electronic cooling *e-Prime—Adv. Electr. Eng. Electron. Energy* **1** 100009
[2] Du L and Hu W 2023 An overview of heat transfer enhancement methods in microchannel heat sinks *Chem. Eng. Sci.* **280** 119081
[3] Li Z, Luo H, Jiang Y, Liu H, Xu L, Cao K, Wu H, Gao P and Liu H 2024 Comprehensive review and future prospects on chip-scale thermal management: core of data center's thermal management *Appl. Therm. Eng.* **251** 123612
[4] Yang B, Chu J, Mitani T and Shinohara N 2021 High-power simultaneous wireless information and power transfer system based on an injection-locked magnetron phased array *IEEE Microw. Wirel. Compon. Lett.* **31** 1327–30
[5] Kenji S and Xiaobo Z 2021 Semiconductor optical amplifier and gain chip used in wavelength tunable lasers vol 19
[6] Dong H, Ruan L, Wang Y, Yang J, Liu F and Guo S 2021 Performance of air/spray cooling system for large-capacity and high-power-density motors *Appl. Therm. Eng.* **192** 116925
[7] Gupta N K, Tiwari A K and Ghosh S K 2018 Heat transfer mechanisms in heat pipes using nanofluids—A review *Exp. Therm. Fluid Sci.* **90** 84–100
[8] Shah J M, Crandall T and Tuma P E 2023 Chip level thermal performance measurements in two-phase immersion cooling *J. Electron. Packag.* **145** 041101
[9] Kadam S T and Kumar R 2014 Twenty first century cooling solution: microchannel heat sinks *Int. J. Therm. Sci.* **85** 73–92
[10] Van Erp R, Soleimanzadeh R, Nela L, Kampitsis G and Matioli E 2020 Co-designing electronics with microfluidics for more sustainable cooling *Nature* **585** 211–6
[11] Smakulski P and Pietrowicz S 2016 A review of the capabilities of high heat flux removal by porous materials, microchannels and spray cooling techniques *Appl. Therm. Eng.* **104** 636–46
[12] Laser D J and Santiago J G 2004 A review of micropumps *J. Micromech. Microeng.* **14** R35–64
[13] Iverson B D and Garimella S V 2008 Recent advances in microscale pumping technologies: a review and evaluation *Microfluid. Nanofluid.* **5** 145–74
[14] Yang C-Y, Yeh C-T, Wang P-K, Liu W-C and Kung E Y-C 2010 An *in-situ* performance test of liquid cooling for a server computer system *2010 5th Int. Microsystems Packaging Assembly and Circuits Technology Conf. 2010 5th Int. Microsystems, Packaging, Assembly and Circuits Technology Conf. (IMPACT)* (IEEE) pp 1–4
[15] Li H, Liu J, Li K and Liu Y 2021 A review of recent studies on piezoelectric pumps and their applications *Mech. Syst. Signal Process.* **151** 107393
[16] Wu R, Duan B, Liu F, Wu H, Cheng Y and Luo X 2017 Design 0/a hydro-dynamically levitated centrifugal micro-pump for the active liquid cooling system *Int. Conf. Electronic Packaging Technology* (IEEE) pp 402–6
[17] Amy C *et al* 2017 Pumping liquid metal at high temperatures up to 1673 kelvin *Nature* **550** 199–203
[18] Zhou Y and Amirouche F 2011 An electromagnetically-actuated All-PDMS valveless micropump for drug delivery *Micromachines* **2** 345–55
[19] Chia B T, Liao H-H and Yang Y-J 2011 A novel thermo-pneumatic peristaltic micropump with low temperature elevation on working fluid *Sens. Actuators Phys.* **165** 86–93
[20] Mousoulis C, Ochoa M, Papageorgiou D and Ziaie B 2011 A skin-contact-actuated micropump for transdermal drug delivery *IEEE Trans. Biomed. Eng.* **58** 1492–8
[21] Nguyen T T, Goo N S, Nguyen V K, Yoo Y and Park S 2008 Design, fabrication, and experimental characterization of a flap valve IPMC micropump with a flexibly supported diaphragm *Sens. Actuators Phys.* **141** 640–8
[22] Ma H K, Chen R H and Hsu Y H 2015 Development of a piezoelectric-driven miniature pump for biomedical applications *Sens. Actuators Phys.* **234** 23–33
[23] Feng G-H and Kim E S 2004 Micropump based on PZT unimorph and one-way parylene valves *J. Micromech. Microeng.* **14** 429–35
[24] Munas F R, Melroy G, Abeynayake C B, Chathuranga H L, Amarasinghe R, Kumarage P, Dau V T and Dao D V 2018 Development of PZT actuated valveless micropump *Sensors* **18** 1302
[25] Luo X, Liu T and Hu R 2025 A micropump and electronic device with fully enclosed bearings, Chinese patent application number: 202510561076.X
[26] Duan B, Guo T, Luo M and Luo X 2014 A mechanical micropump for electronic cooling *14th Intersociety Conf. on Thermal and Thermomechanical Phenomena in Electronic Systems (Itherm) 2014 IEEE Intersociety Conf. on Thermal and Thermomechanical Phenomena in Electronic Systems (Itherm)* (IEEE) pp 1038–42